AGU PUBLICATIONS

JGR

Journal of Geophysical Research: Space Physics

RESEARCH ARTICLE
10.1002/2015JA021481

Key Points:
- Simultaneous observations of the ionospheric OCB
- Mapping location offsets related to the solar cycle
- High-density EUV ionized plasma causes beam refraction

Correspondence to:
X.-C. Chen,
xiangcai.chen@unis.no

Citation:
Chen, X.-C., D. A. Lorentzen, J. I. Moen, K. Oksavik, and L. J. Baddeley (2015), Simultaneous ground-based optical and HF radar observations of the ionospheric footprint of the open/closed field line boundary along the geomagnetic meridian, *J. Geophys. Res. Space Physics*, *120*, 9859–9874, doi:10.1002/2015JA021481.

Received 22 MAY 2015
Accepted 19 OCT 2015
Accepted article online 10 NOV 2015
Published online 12 NOV 2015

Simultaneous ground-based optical and HF radar observations of the ionospheric footprint of the open/closed field line boundary along the geomagnetic meridian

X.-C. Chen[1,2,3], D. A. Lorentzen[1,2], J. I. Moen[1,3], K. Oksavik[1,2], and L. J. Baddeley[1,2]

[1]Department of Arctic Geophysics, University Centre in Svalbard, Longyearbyen, Norway, [2]Birkeland Centre for Space Science, Department of Physics and Technology, University of Bergen, Bergen, Norway, [3]Department of Physics, University of Oslo, Oslo, Norway

Abstract Previous studies have confirmed that the equatorward boundaries of OI 630.0 nm auroral emissions and broad Doppler spectral widths in Super Dual Auroral Radar Network (SuperDARN) data, the so-called spectral width boundary (SWB), are good empirical proxies for the dayside open/closed field line boundary (OCB) in the ionosphere. However, both observational techniques are associated with mapping errors. SuperDARN uses a virtual height model for mapping, but it is not well known how the mapping error responds to a changing background ionosphere or transient reconnection events. Optical instruments, such as the meridian-scanning photometers, have high spatial resolution near zenith, where the mapping error due to the assumed OI 630.0 nm auroral emission height becomes small by comparison. In this work, an adjusted method is introduced to identify the SWB, which does not require temporal smoothing across several scans. The difference in latitude between the SWB, as identified using this method, and the simultaneously observed OI 630.0 nm auroral emission boundary along a common line of sight is compared. Utilizing the OI 630.0 nm boundary as a reference location, we present two case studies observed at different levels of solar activity. In both instances the latitude offset of SWB from the reference location is discussed in relation to the background ionospheric electron density. The compared results indicate that the intake of high-density solar extreme ultraviolet ionized plasma from subauroral latitudes causes a refraction of the HF radar beam path, which results in an overestimation of range mapping. The adjusted method would thus be a useful tool for identifying the OCB under changing ionospheric conditions in the cusp region.

1. Introduction

The cusp is a region where the solar wind has direct access to the ionosphere by magnetic reconnection. The ionospheric plasma convection in this region is strongly modulated by the interplanetary magnetic field (IMF) components [e.g., *Dungey*, 1961; *Cowley and Lockwood*, 1992]. Cusp optical signatures at 630.0 and 557.7 nm are associated with dayside reconnection activity and have been extensively investigated [e.g., *Sandholt et al.*, 1998]. The OI 630.0 nm auroral emissions, with an excitation lifetime of about 110 s and luminosity in the order of kilo-Rayleigh, are readily produced by de-excitation of the ^1D state of atomic oxygen. Since the cusp electron auroral signatures can be easily identified, the equatorward boundary of the OI 630.0 nm emission can act as a good proxy for the ionospheric footprint of dayside magnetic reconnection [e.g., *Lorentzen et al.*, 1996; *Lockwood*, 1998; *Moen et al.*, 1998]. The precipitating soft electrons also produce 10 m scale plasma irregularities at kilometer-scale electron density gradients, as was recently confirmed by high-resolution ICI-2 sounding rocket data [*Moen et al.*, 2012; *Oksavik et al.*, 2012]. Strong coherent backscatter from these irregularities, at the Bragg scale and transverse to the magnetic field, can be monitored by the Super Dual Auroral Radar Network (SuperDARN) HF radars in the polar ionosphere [e.g., *Greenwald et al.*, 1995; *Chisham et al.*, 2007]. The de-correlation time of the modulus of the autocorrelation function (ACF), derived from the measured backscattered signal, can be utilized to obtain measurements of the spectral width of the Doppler velocity. The magnitude of the width can be interpreted as a manifestation of plasma characteristics of the scattering region itself. Thus, a transition from narrow to broad spectral widths has been utilized to investigate the location of ionospheric boundaries [e.g., *Baker et al.*, 1995; *Yeoman et al.*, 1997]. The intimate co-location of the equatorward edge of the HF radar cusp and the cusp auroral emission has been

extensively studied [e.g., *Rodger et al*., 1995; *Yeoman et al*., 1997; *Milan et al*., 1999; *Moen et al*., 2001]. *Rodger et al*. [1995] showed that the HF cusp signatures were located on average 0.5° equatorward of the optical cusp when the IMF B_z is negative, which agrees with the results of *Oksavik et al*. [2004b]. However, *Milan et al*. [1999] and *Moen et al*. [2001] found that the equatorward boundaries of the optical cusp were, on average, located at slightly lower latitudes than the HF radar cusp. This was still evident even when *Moen et al*. [2001] tried to compensate for mapping errors by using different emission altitudes for the aurora.

Current mapping of HF radar returns uses the assumption that the radio wave raypath has the same slant range as propagation to a virtual height (400 km at far ranges), which does not directly take into account the prevailing HF propagation conditions [*Baker et al*., 1986]. This introduces a problem with accurate mapping of ionospheric backscatter. Decreasing the mapping error has important implications for studies of auroral plasma signatures on small and mesoscale sizes. For example, *Moen et al*. [2008b] discussed the relationship of thin Birkeland current arcs associated with reversed flow channels in the winter cusp/cleft ionosphere. The typical reversed flow event (RFE) is a 100–200 km wide flow channel that is longitudinally elongated and has a flow direction that is opposite to the background convection [*Rinne et al*., 2007]. These mesoscale events in the cusp region have been extensively observed by the European Incoherent Scatter (EISCAT) Svalbard radar (ESR) [e.g., *Oksavik et al*., 2004a, 2005; *Moen et al*., 2008b]. *Oksavik et al*. [2011] also reported RFEs seen by SuperDARN HF radar. To study the relationship between the RFE and Birkeland currents, they used a ground range offset of 140 km to align the HF radar echoes with the optical signatures.

The range determination is based on time-of-flight of HF radar backscatter returns. Assessing the accuracy of the mapping of HF echoes has previously been studied by ray-tracing simulation [e.g., *Villain et al*., 1984; *Baker et al*., 1986; *Liu et al*., 2012], and several studies have indicated that accurate determination of the propagation path at far ranges is difficult, especially in the high-latitude cusp region [e.g., *Lei et al*., 2006; *Zhang et al*., 2007; *Moen et al*., 2008a]. An absolute evaluation of range accuracy was first performed by *Yeoman et al*. [2001]. By using the high-power RF facility (ionospheric heater) operated by EISCAT at Tromsø, which is at a known, fixed location, *Yeoman et al*. [2001] found the standard virtual height for backscatter ground range to be accurate to within 60 km at a one and a half hop propagation path from Pykkvibær to Tromsø. Based on statistical analysis of ionospheric HF radar backscatter elevation angles, a new virtual height model was developed by *Chisham et al*. [2008] to improve the current echo mapping both at near and far ranges. Their results showed that the scattering locations were overestimated by ~100–200 km at far ranges when using the standard virtual height model (see their Figure 5, bottom). They suggested that the large variation in the uncertainty of the offset should be a result of the different propagation conditions due to the changes in the ionospheric peak electron density. Subsequently, *Yeoman et al*. [2008] quantitatively tested this new virtual height model by using the ionospheric heaters at Tromsø and Longyearbyen (Space Plasma Exploration by Active Radar). Their results (see Figure 4c (*iv*) in *Yeoman et al*. [2008]) showed that the one and a half hop pseudo-virtual height model of *Chisham et al*. [2008] prominently reduced the mapping error, but there still exists a range difference of about 60 km. By comparing the two events from different years of artificially induced backscatter echoes along the same path, *Yeoman et al*. [2008] suggested that the solar cycle is playing a role in the increased range errors.

All these previous studies imply that the mapping uncertainties are not only an effect of the dayside ionospheric reconnection, but also an effect of the changing background ionosphere density, which relates to the transport of solar extreme ultraviolet (EUV) ionized plasma and solar cycle. How both factors contribute to the mapping error is still not fully understood. Svalbard is very well situated for dayside cusp auroral observations, and the SuperDARN Finland radar overlaps the field-of-view of the optical instruments, including all-sky imagers and meridian-scanning photometers (MSPs). The high-latitude ground-based instruments offer a unique opportunity to monitor dayside reconnection activity and the motion of the polar cap boundary in near real-time. The motivation for this paper is to investigate how the mapped HF radar cusp boundary responds to the background ionosphere and its relationship to the cusp particle precipitation boundary. An overview of the instrumentation is given in section 2. The methods for determining the location and motion of the OI 630.0 nm auroral emission and the HF radar Doppler spectral width boundaries (SWBs) are introduced in section 3. In section 4, two case studies are used to investigate the offset of the auroral boundary with SWB using these methods, and the boundary discrepancy is discussed in section 5.

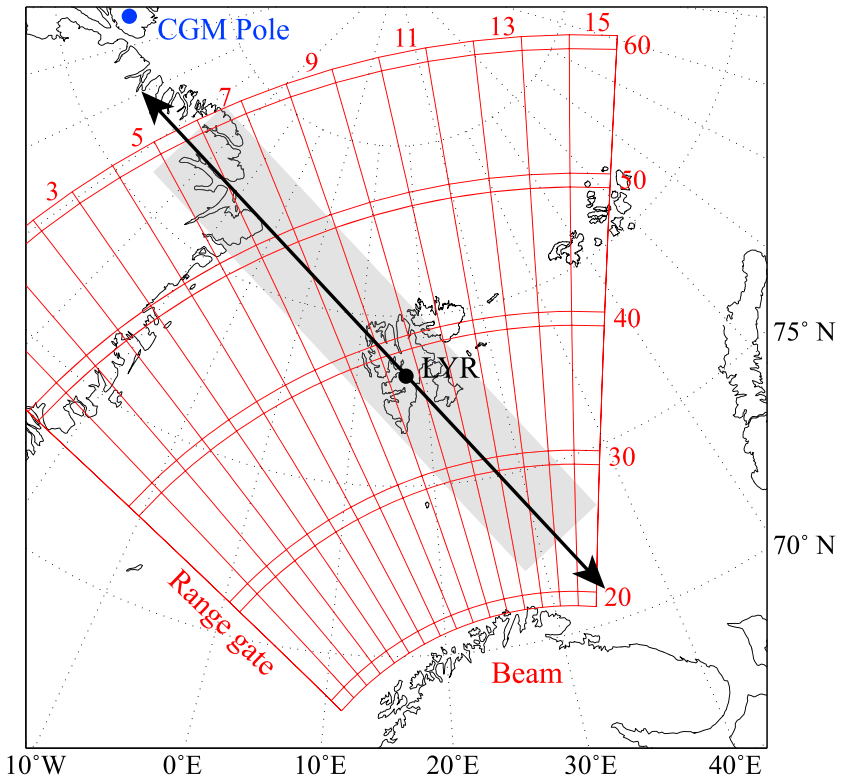

Figure 1. Fields of view of the MSP and the SuperDARN Finland radar in geographic coordinates. The black dot indicates the location of Longyearbyen and intersects with the SuperDARN Finland radar beam 9. The shaded area represents the adjacent range gates along the MSP line, as defined by the algorithm.

2. Instrumentation

2.1. Auroral Data From the Longyearbyen MSP

The MSP instrument, located at the Kjell Henriksen Observatory in Longyearbyen, Svalbard (LYR, geographic coordinates: 78.2°N, 16.0°E; see Figure 1), provides high temporal and spatial resolution optical observations near zenith. There are five channels, including the OI 630.0 nm red and OI 557.7 nm green auroral emissions. A rotating mirror is used to scan along the geomagnetic meridian plane (31° west of geographic north) from north to south. Each channel consists of a cooled photomultiplier tube and tilting narrow band-pass interference filter in order to record both the peak and background emissions [*Romick*, 1976]. The intensity is absolutely calibrated using a NIST traceable light-emitting diode calibration source. The MSP has an angular resolution of 1° and a temporal resolution of 16 s (one full peak minus background scan).

2.2. HF Backscatter Data From the SuperDARN Finland Radar

The Cooperative UK Twin Located Auroral Sounding System Finland radar, which is one of the SuperDARN radars, is located at Hankasalmi (62.3°N, 26.6°E). The 16 phased antenna arrays, operating at frequencies between 8 and 20 MHz, cover 52° in the azimuthal direction starting from 12° west of geographic north. In the current study, the normal scan mode employed a dwell time of 7 s at each beam for a full 2 min scan. The 75 range gates of each beam direction were sampled using a pulse length of 300 μs, which corresponds to 45 km long range gates, with the first range gate located at a distance of 180 km. When the transmitted radio wave, $\mathbf{k}_r$, becomes orthogonal to the local magnetic field and satisfies the Bragg scatter conditions with the ionospheric wave vector $\mathbf{k}$ (i.e., $\mathbf{k} = \pm 2\mathbf{k}_r$), echoes from field-aligned plasma irregularities will be backscattered and subsequently received at the radar site. Using a multipulse sequence to produce multilag complex ACFs, the HF radar backscattered power, the line-of-sight Doppler velocity of the plasma irregularities, and the Doppler spectral width within the scattered volume can be processed [*Greenwald et al.*, 1995]. Beam 9 of the SuperDARN Finland radar intersects with the Longyearbyen MSP instrument at ~1890 km ground range (see Figure 1).

2.3. IMF and Solar Wind Data

The solar wind and IMF data monitored by the ACE and WIND satellites will be used in the two case studies, respectively. Both spacecraft were located upstream of the magnetosphere during the time intervals studied. The transit time of the solar wind from the satellite to the cusp ionosphere was estimated using the equation given by *Liou et al*. [1998]. The expected times for traversing the magnetosheath and the subsequent Alfvén wave transit time to reach the ionosphere are 5 and 2 min, respectively [*Lockwood et al*., 1989].

3. Boundary Identification Techniques

3.1. Equatorward Boundary of the OI 630 nm Auroral Emissions

The emission altitude of OI 630.0 nm auroral emissions is notoriously difficult to determine. The OI 630.0 nm optical features are normally mapped using an assumed peak emission altitude of ~220–250 km. The term "emission altitude" refers to a best estimate of the peak emission height, where significant excitation by particle impact of precipitating electrons and by thermal excitation of the ambient electron gas and dissociative recombination of O_2^+ ions occur [e.g., *Rees*, 1989; *Lockwood et al*., 1993]. The $O(^1D)$ state has a theoretical lifetime of ~110 s in the *F* region. The presence of neutral wind and ion drag causes the OI 630.0 nm auroral emission to become somewhat diffuse. *Lorentzen et al*. [1996] detected a demarcation of the cusp soft electron precipitation, by comparing the equatorward boundary of the OI 630.0 nm red auroral emissions with a maximum intensity gradient along the MSP meridian and data from a traversing sounding rocket. Soft electron precipitation having energies at 0.1–1 keV [*Newell and Meng*, 1988] is a good indicator of open magnetic field lines and corresponds to auroral emissions dominated by the OI 630.0 nm emission (i.e., a Rayleigh intensity ratio 630.0/557.7 $>$ 1) [e.g., *Rees*, 1963; *Lorentzen and Moen*, 2000].

Based on a predefined reference cusp aurora produced by the GLOW model [*Solomon et al*., 1988], a simulation for obtaining the magnetic latitude of the open/closed line boundary (OCB) from 630.0 nm auroral emissions in MSP data was performed by *Johnsen et al*. [2012]. Through selected neutral atmosphere (MSIS-90 model) parameters and at least one electron density profile, the GLOW model can create an effective two-dimensional volume emission rate profile of the 630.0 nm emission by inputting electron impact excitation, airglow, and thermal excitation (see *Johnsen et al*. [2012] for more details). Using the modeled volume emission rate, the mapping height as a function of MSP scan angle was found together with a set of equations describing the mapping error. The validity of the method was then tested utilizing a number of case studies, for which a direct comparison could be made with data from satellites traversing the region [*Johnsen and Lorentzen*, 2012]. Since the same instrument is utilized in the present study, this constructed reference altitude for transforming the auroral emission boundary into ground range and Altitude Adjustment Corrected Geomagnetic Coordinates [*Baker and Wing*, 1989] will be used to allow a comparison to the HF radar SWB.

3.2. Equatorward Boundary of the Spectral Width

Many studies have revealed that the high-latitude broad Doppler spectral width can be used as an indicator for the cusp region ionosphere [e.g., *Baker et al*., 1995; *Rodger et al*., 1995; *Moen et al*., 2001; *Villain et al*., 2002], even though the interpretation of the broad spectral width is still elusive. *Baker et al*. [1995] suggested that the distribution of spectral widths in the cusp region could be approximated by a Gaussian distribution centered on ~220 m/s. *Moen et al*. [2001] used this criterion to determine that the HF radar SWB was closely correlated to the equatorward boundary of the OI 630.0 nm cusp aurora.

Different methods have been developed to identify the SWB in the cusp region, including fitting a linear function of magnetic latitude and magnetic longitude through the set of range gate points [e.g., *Pinnock and Rodger*, 2001], and temporally averaging over three consecutive scans and median of three adjacent beams [*Chisham et al*., 2001]. The different algorithms to accurately determine the SWB were assessed by *Chisham and Freeman* [2003]. They concluded that spatial and temporal smoothing of the spectral width data (i.e., median filtering) along the beam can increase the boundary determination accuracy to over 95% and the average boundary error to much less than one range gate. However, this method is built at the cost of the temporal resolution of the boundary motion. In addition, the Finland radar scan beams are not aligned completely along the meridian plane of the MSP (see Figure 1). As later pointed out by *Chisham et al*. [2005b], the gradient in the large-scale ionospheric convection pattern becomes more unreliable for beams

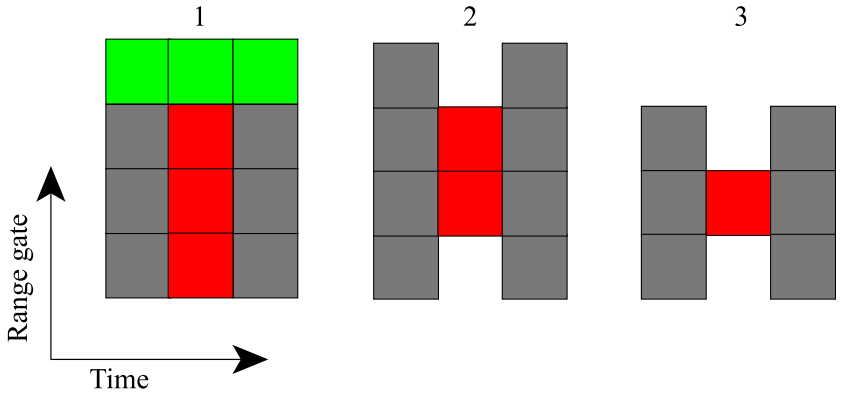

Figure 2. An illustration of the algorithm utilized to identify the SWB. The columns 1-2-3 indicate how the SWB is identified as the threshold criteria for different numbers of range gates (which are aligned along the MSP line) is exceeded, as a function of scan time. See text for a more detailed description.

away from the meridional direction. To minimize this effect the method presented in this paper utilizes range gates that are not confined to a single radar beam but are chosen so that they are co-located along the MSP line.

To determine the location and motion of the SWB in this study, ground scatter will be eliminated using the criteria of *Baker et al*. [1988]. Subsequently, the range gates fitting the MSP orientation and their adjacent range gates will be selected (see Figure 1, gray area) before the application of the median filter technique. For a spectral width $w_{(i,\ j)}$ at range gate i and beam j along the MSP line, the adjacent range gates correspond to $w_{(i-1,j-1)}$ and $w_{(i+1,\ j+1)}$, respectively. This process can also be applied to backscatter power and velocity.

An illustration of the automatic boundary identification algorithm is shown in Figure 2. Each column indicates the consecutive dwell times of the median filtered range gates along the MSP line, as a function of scan time. The red boxcar represents spectral width values greater than the threshold (e.g., 200 m/s), and the green and gray cells show time consecutive range gates. The algorithm will be applied to range gates identified as lying along the MSP meridian, from the most equatorward to the most poleward. When three range gates are above the threshold (i.e., indicated by the range gates marked in red in situation 1, $w_{(i,\ j)}$, $w_{(i+1,\ j)}$, and $w_{(i+2,\ j)}$), and at least 50% of the poleward adjacent range gates (range gates marked in green, $w_{(i+3,\ j-1)}$, $w_{(i+3,\ j)}$ and $w_{(i+3,\ j+1)}$) are above the threshold, the first equatorward gate will be identified as the boundary. This is similar to the method of *Chisham and Freeman* [2003]. Conversely, when the number of the poleward adjacent range gate values above the threshold is below 50%, the analysis will consider whether at least 50% of the consecutive range gates (marked in gray) are above the threshold. If both criteria are not satisfied, the analysis will shift one range gate poleward (i.e., $w_{(i+1,\ j)}$, $w_{(i+2,\ j)}$, and $w_{(i+3,\ j)}$) and continues the test until both criteria are satisfied. In the situation when only two adjacent or one single range gate (situations 2 or 3 in Figure 2) is above the threshold, at least 50% of the consecutive range gates (marked in gray) must be above the threshold. If these criteria are not met, the analysis will continue to step poleward until the criteria are satisfied. If no criterion is satisfied, the algorithm will record that no boundary can be identified.

In the cases where no data are recorded in a particular range gate, an extra criterion is implemented utilizing the plasma velocity. A typical plasma velocity of ~±1000 m/s would produce a poleward (or equatorward) displacement of about 120 km (i.e., 2–3 range gates) between consecutive full scans (~120 s). Any identified SWB displacements of greater than three range gates between scans (i.e., in 120 s) are thus discounted. This eliminates any false boundary identifications due to lack of data.

In this paper, the raw data were processed using FITACF v1.09. Many factors have a complex convolution effect on the spectral width values [e.g., *Moen et al*., 2001; *Chisham et al*., 2005c; *Ponomarenko and Waters*, 2006, and reference therein]. The studies by *Baker et al*. [1997], *Pinnock et al*. [1999], and *Pinnock and Rodger* [2001] concluded that a spectral width value of 150 m/s should be utilized to define the SWB, whereas a study by *Chisham et al*. [2001] concluded that 250 m/s was a more suitable choice. By studying the factors which determine the spectral width of HF echoes in the high-latitude *F* region, *Ponomarenko et al*. [2007]

found that the spectral width values decrease as the radar operating frequencies increases (i.e., $F = 1/\tau_{corr} \approx 2\pi \cdot f_0 \cdot W/c$, where f_0 is the radar frequency, c is the speed of light, and τ_{corr} is irregularity lifetime). Both case studies used in this study utilize radar frequencies near 10 MHz, and considering that the typical "normalized" spectral width, F, is 40 Hz [*Ponomarenko et al.*, 2007], a spectral width threshold, W, of 200 m/s is applied.

The improved temporal resolution is achieved by applying the median filter across the adjacent range gates in a single 2 min scan to identify the SWB. The previous method [e.g., *Chisham and Freeman*, 2003] utilized additional median filtering across five successive scans before ascertaining the location of the SWB. An additional check utilizing the distribution of spectral width values either side of the SWB, as identified by the algorithm, is also undertaken. The distribution of the spectral width values at six range gates above (below) the identified SWB is found to have a Gaussian (exponential) form (plots not shown), in agreement with the findings of *Chisham and Freeman* [2003]. Additionally, there was no significant overlap between the distributions, adding confidence that the estimated SWB location is not influenced by a significant amount of statistical noise.

4. Observations

4.1. Case Study 1: 01 January 2003

Figures 3a–3c present a range gate versus time plot of backscatter power, line-of-sight velocity, and spectral width obtained along the MSP meridian from 06:00 to 12:00 UT on 1 January 2003. Four intervals are indicated by the vertical lines. An area of elevated backscatter power, enhanced Doppler velocities, and large spectral width is centered on range gates around 35–55 from 06:00 to 10:00 UT. The black curve in each panel represents the SWB as identified using the algorithm. Positive (negative) line-of-sight velocities in Figure 3b are toward (away from) the radar. Transient increases in the line-of-sight velocity, i.e., pulsed ionospheric flows, are a common signature that often starts near the SWB and move into the polar cap, which are intimately associated with poleward moving auroral forms (PMAFs) [e.g., *Milan et al.*, 1999]. The low-latitude prenoon and postnoon return flows are observed equatorward of the SWB in time intervals *I* and *III*, respectively. During the interval *I*, the area of high spectral widths was relatively narrow in latitudinal extent and the SWB moved gradually equatorward. In intervals *II* and *III* the SWB migrates poleward, and the area of high spectral widths extended over a wider range in latitude.

The corresponding observations of the OI 630.0 nm auroral emissions from the MSP are plotted versus time and scan angle in Figure 3d. A series of PMAFs with equatorward boundary intensification and high-latitude rebrightenings are observed, which are consistent with intensified magnetopause reconnection [*Lockwood et al.*, 1989]. The equatorward boundary of the OI 630.0 nm emission is marked by a dashed curve, which is a proxy for the OCB. Two periods of weak auroral intensity around 07:10 and 08:35 UT are approximately consistent with the decreased reconnection electric field, derived from SuperDARN convection velocity data (not shown). Due to the lack of HF radar echoes in time interval *IV*, the comparison of the latitude difference is undertaken from 06:00 to 10:00 UT.

Figure 4a shows IMF data from ACE, which was situated near (242.3, −10.8, 20) R_E in GSM coordinates during the period of interest. The nearly constant solar wind speed of ~420 km/s corresponds to a 63 ± 4 min time shift. The abrupt polarity changes in IMF B_z (i.e., at ~08:35 UT) correspond to modulations in the auroral intensities and are additionally used to verify the applied time delay. IMF B_x was mostly positive. IMF B_y was strongly positive but gradually decrease from ~7 nT at prenoon magnetic local time (MLT) to ~3 nT at postnoon MLT (noon MLT ≈ 08:50 UT at LYR). B_z was predominantly negative throughout the interval, which is favorable for subsolar reconnection [*Sandholt et al.*, 1998]. The corresponding IMF clock angle, defined as $\theta = \tan^{-1}(|B_y/B_z|)$ for $B_z > 0$ and $\theta = 180° - \tan^{-1}(|B_y/B_z|)$ for $B_z < 0$ in the GSM *y-z* plane, varied between 60° and 135° and is denoted by the blue curve in Figure 4b.

The difference in latitude between the HF radar SWB and the OI 630.0 nm emission boundary is shown in Figure 4b (pink line with black dots). Latitude uncertainties, which arise from the auroral altitude model, are shown as red error bars. The dashed horizontal line at zero degree latitude difference represents the location of the derived 630.0 nm boundary. Most of the time the HF radar SWB is located significantly poleward of the auroral boundary (on average ~1.55° or ~170 km, peaking at ~2.8°). From 06:00–08:50 UT the latitude

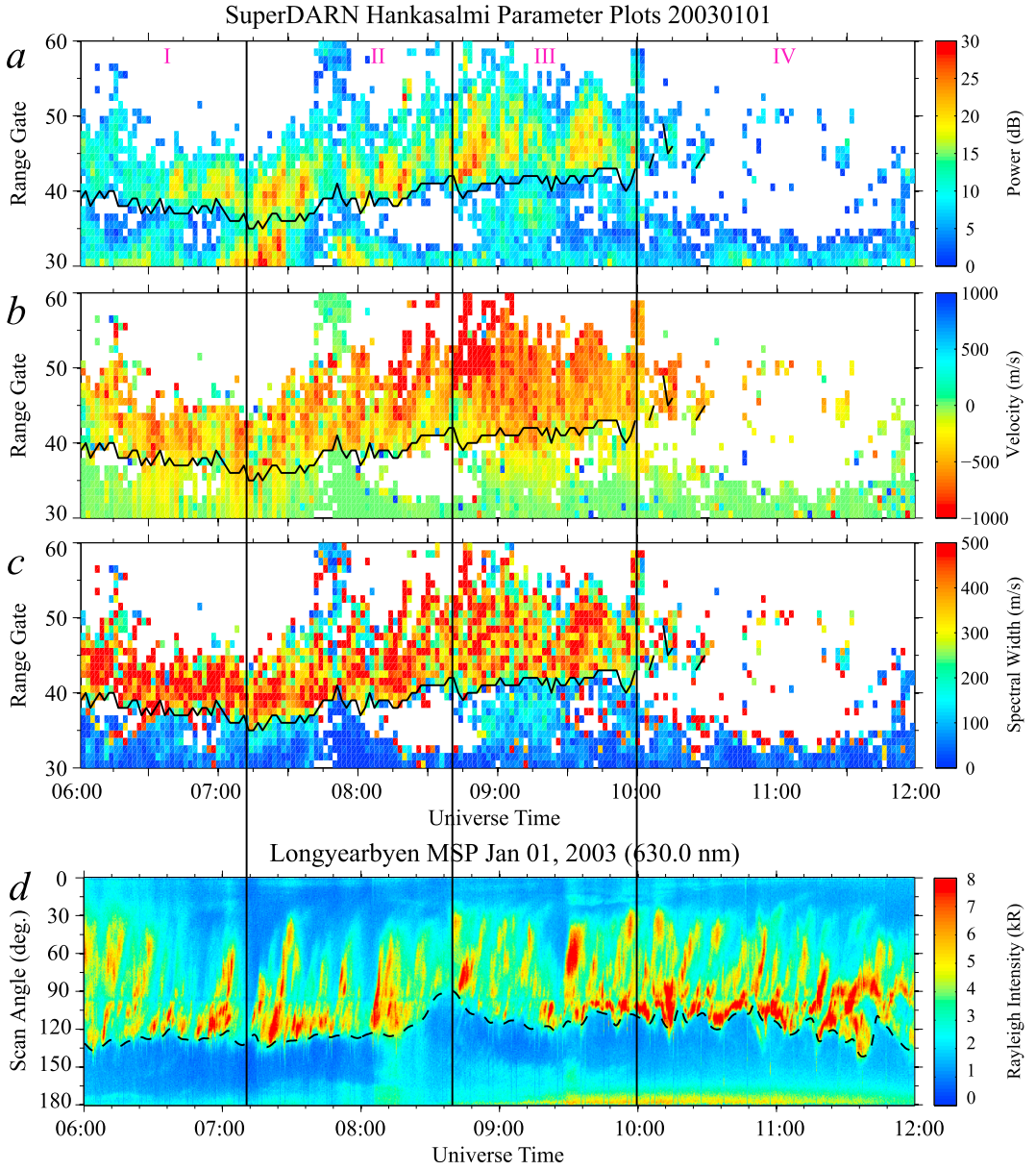

Figure 3. (a–c) Range gate versus time plots on 1 January 2003 of HF radar backscatter aligned along the MSP meridian. From top to bottom the parameters are backscatter power, line-of-sight velocity, and spectral width. The black curve in all panels is the SWB obtained by the automatic search algorithm. (d) The OI 630 nm auroral emissions versus MSP scan angle, as a function of time. The dashed curve represents the identified auroral emission boundary.

difference between the two boundaries varies between ~0° and ~2.5°, with an average difference of ~1.23°. During this time the IMF clock angle is also varying significantly between 60° and 135°. The latitude differences during this time are likely to be associated with the multiple southward turnings in the IMF B_z component. At ~08:50 UT (i.e., close to noon MLT), there is an increase in latitudinal difference between the two boundaries (to an average of 2.28°), which coincides with a period of stable IMF clock angle (~115°). The negative B_z component indicates that subsolar reconnection is ongoing. This, coupled with the magnitude and polarity of the IMF B_y component, is consistent with an ionospheric convection pattern with the throat region located toward the duskward side.

The meridian line-of-sight Doppler velocities along the MSP line, with error bars representing 1 standard deviation, are shown in Figure 4c. The westward plasma motion, and thus the position of the convection

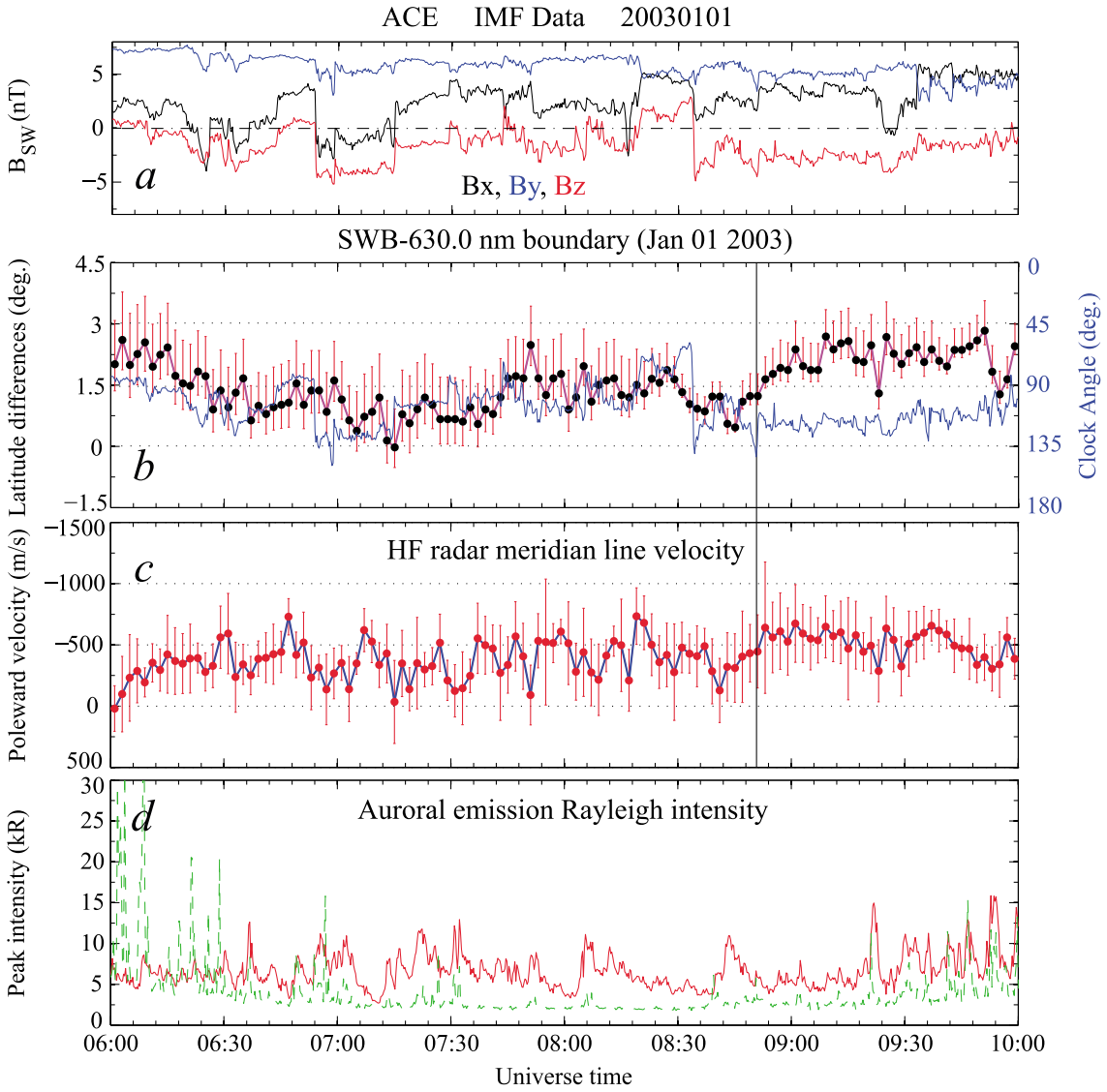

Figure 4. (a) IMF parameters from the ACE satellite measured in GSM coordinates on 1 January 2003 and time shifted by 65 min to correspond with ground-based observations from 06:00 to 10:00 UT. (b) Difference in latitude between the HF radar SWB and the OI 630 nm auroral boundary versus time indicated by the pink line with black dots and red error bars. The IMF clock angle is overlaid as a blue curve. (c) The poleward line-of-sight Doppler velocity along the MSP meridian. (d) The red and green lines mark the peak intensities of the 630.0 and 557.7 nm emissions, respectively.

throat region within the radar field-of-view, is modulated by the IMF B_y-related tension force. The enhanced poleward velocity has an average recurrence period of 2–10 min, and each event is roughly followed by a PMAF. However, from ~08:50 UT more stable poleward velocities of ~550 m/s are observed (indicated by a vertical line), which is consistent with the observed plasma flow direction now being aligned to the throat region on the duskward side. To illustrate the temporal changes in the auroral particle energy spectra, the observed peak intensities of the 630.0 nm (solid red line) and 557.7 nm (dash green line) emissions were plotted in Figure 4d. The emission intensity of the 630.0 nm (red) aurora exceeds that of the 557.7 nm (green) aurora from 06:30 UT, indicating cusp like particle precipitation. The more intense green auroral emissions (which occur before 06:30 UT) are indicative of higher energetic particle precipitation. The presence of this higher energy population will lower the 630.0 nm peak emission height to below the model reference height, resulting in an underestimation of the real auroral emission boundary. This could explain the large difference in latitude between the HF radar SWB and the OI 630.0 nm equatorward boundary at the start of the interval.

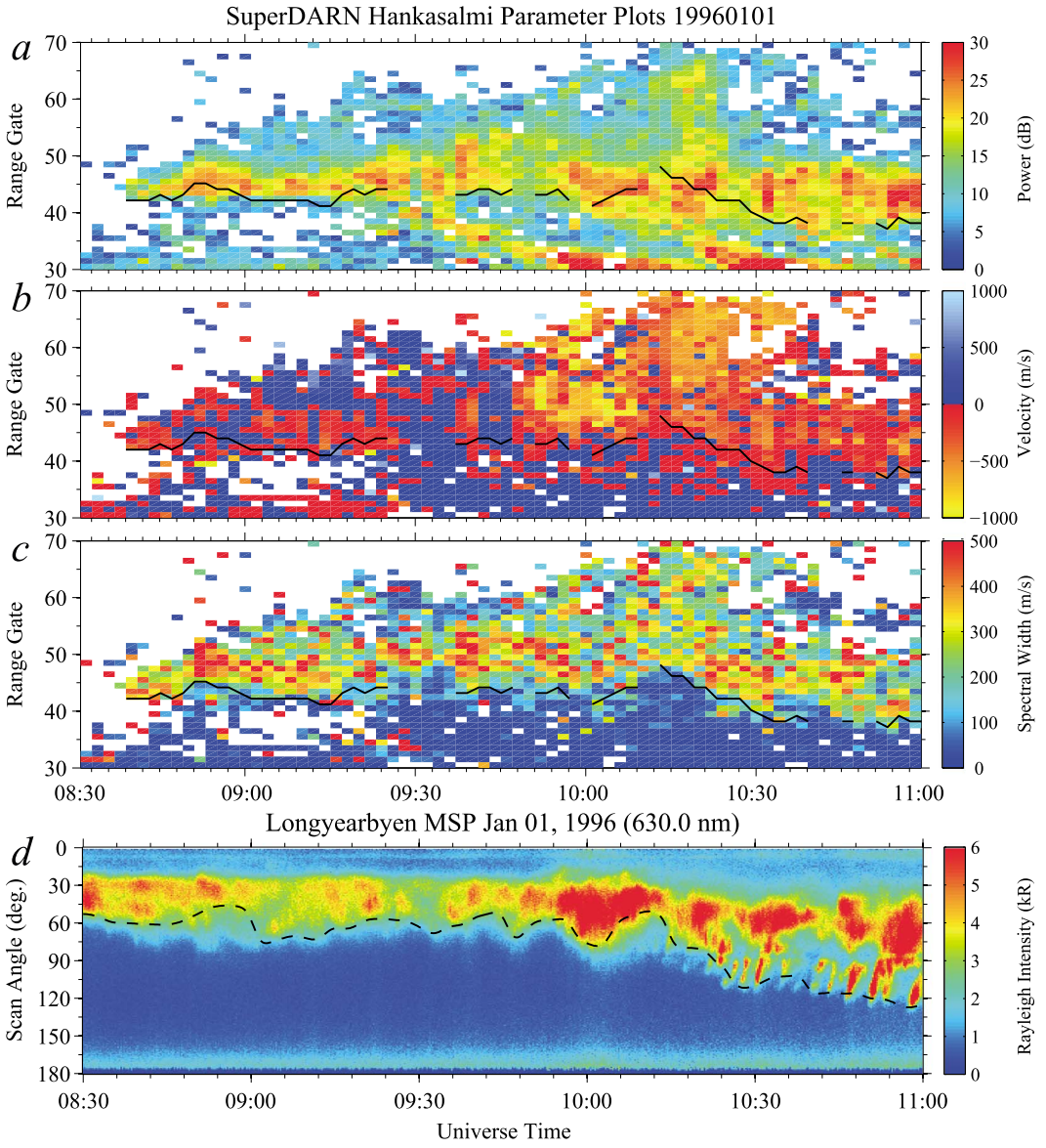

Figure 5. (a-c) Range gate versus time plots on 1 January 1996. (d) The corresponding OI 630 nm auroral observation versus MSP scan angle and time, with the black dashed curve indicating the emission boundary.

4.2. Case Study 2: 01 January 1996

Simultaneous HF radar ionospheric and OI 630.0 nm aurora emission observations from 08:36 to 11:00 UT on 01 January 1996 are shown in Figure 5. The identified SWB is shown by the overlaid black curve. The intermittent nature of the curve is a result of the identification criteria detailed in section 3.2. In contrast to the case study presented in the previous section, with the auroral emission location situated at either side of the zenith (as viewed from the MSP), the cusp aurora is mostly situated toward the northern horizon before 09:50 UT (~13:00 MLT). The high-latitude cusp aurora for IMF B_z northward (see Figure 6a) is called "type 2" aurorae by *Sandholt et al.* [1998]. Its poleward and equatorward boundaries depend on the IMF B_y and B_x polarities and have related plasma convection and field-aligned current (FAC) patterns in the cusp region [*Øieroset et al.*, 1997]. In Figure 5b, it should be noted that a transition between two different plasma convection patterns occurred at ~09:50 UT. Before that, flow shears near the SWB can be associated with enhanced backscatter power, spectral widths, and coincident OI 630.0 nm auroral emissions (shown in Figure 5d). As the clockwise vorticity is consistent with an upward FAC, i.e., intense aurora, the counterclockwise vorticity around range gate 50 should be related to the poleward boundary of the aurora, consistent with the RFEs

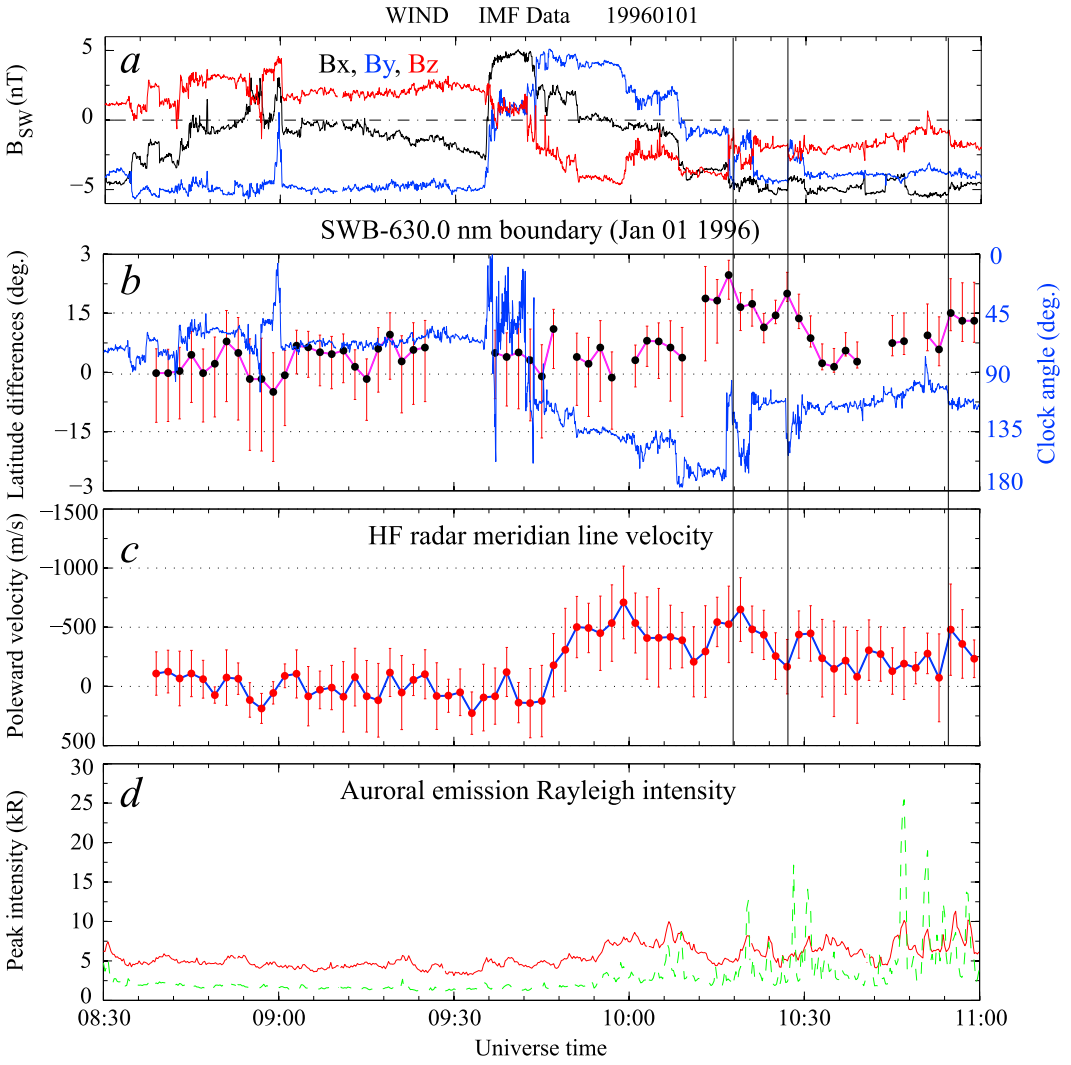

Figure 6. (a) IMF components on 1 January 1996 from the WIND satellite using a propagation delay of 27 min. (b) The difference in latitude between the HF radar SWB and the OI 630 nm auroral boundary versus time, indicated by the pink line with black dots and red error bars. The IMF clock angle overlaid as a blue curve. (c) The poleward line-of-sight Doppler velocity along the MSP meridian. (d) Peak intensities of the red 630.0 and green 557.7 nm auroral emissions plotted as a solid red line and a dashed green line, respectively.

observations by *Oksavik et al.* [2011]. From 10:15 to 11:00 UT a sequence of 14 PMAFs, which form in the equatorward region and subsequently move poleward, is observed in the MSP data. With the concurrent high-latitude diffuse auroras, these emissions are typical dayside auroral bifurcation events during B_y-dominated IMF [*Sandholt et al.*, 2001], indicating simultaneous lobe and magnetopause reconnection [*Sandholt et al.*, 1998]. The open-closed boundary is marked as a black dashed curve at the equatorward boundary of the aurora in Figure 5d.

Figure 6a shows the IMF components from the WIND spacecraft at (87, −23, 9) R_E in GSM coordinates. The propagation delay is estimated to be 27 min, which is consistent with the IMF B_z southward turning and resulting strong intensification of the aurora and enhanced poleward line-of-sight velocity at 09:50 UT (see Figure 6c). There is a change in the IMF B_x and B_y components from negative to positive which occurs at approximately 10 min before the B_z southward turning. B_y was negative, except for a ~35 min interval ending around 10:10 UT. The difference in latitude between the HF radar SWB and the OI 630.0 nm auroral boundary shown in Figure 6b indicates that the SWB is, on average, ~0.51° or ~56 km poleward of the auroral emission boundary, peaking at 2° and with a minimum at −0.5°, respectively. It is on average almost 1° smaller than the

case presented in the previous section. To investigate the possible effects due to the polarities of the IMF components, the latitude difference before and after the change in polarity of the IMF B_z component (which occurred at 09:50 UT) was compared. The mean latitude difference is 0.39° for B_z northward, while it is 0.76° for B_z southward. The average poleward Doppler velocity along the meridian line (Figure 6c) is also smaller under B_z northward conditions. In addition to the change in polarity of the B_z component, there is also a polarity change in the B_y component at this time. The combination of these changes will result in an increased reconnection electric field and a movement of the throat region of the ionospheric convection pattern from the dawnside toward the duskside. This manifests itself in the sharp increase in poleward velocity as the flows become more directed along the HF radar beam.

In Figure 6b, it is seen that there are several gaps in the HF radar SWB between 09:26 to 10:50 UT. A possible explanation is given by *Oksavik et al*. [2012], who suggest that significant irregularities may not be present if the plasma is stable to irregularity growth. It should be noted that almost all these HF radar SWB intermittences corresponds to equatorward movement of the OI 630.0 nm auroral boundary, which means an expansion of the polar cap boundary with an intake of newly open flux, which in turn would alter the propagation condition for HF radio waves.

5. Discussion

An adjusted approach for identifying the ionospheric SWB by HF radar with high-temporal resolution is described in this paper. Compared to the traditional determination methods [e.g., *Milan et al*., 1999; *Moen et al*., 2001; *Pinnock and Rodger*, 2001; *Chisham and Freeman*, 2003], more criteria are used in order to effectively eliminate the off-meridional effect [*Chisham et al*., 2005b] and to avoid ambiguous boundary identification.

5.1. Variability With Solar Cycle

The two events presented in this paper utilized the same radar scan mode and transmitter frequency. Additionally, they occurred on 1 January but from different years (2003 and 1996) during a solar cycle. The latitudinal difference between the SWB and the auroral boundary was, on average, ~1° larger for the first event (2003) than the second event (1996). This suggests that solar cycle variations in the background ionospheric density may play a role in the raypath of the HF radar signal. In 2003 the 3 month average solar flux at 10.7 cm wavelength was 150 (75% of the maximum in solar cycle 23). In 1996 it was 65 (32.5% of the maximum in solar cycle 23). The high-latitude ionosphere receives higher solar flux during solar maximum, i.e., more photoelectric ionization. The resulting peak electron density in the *F* region is typically higher (and occurs at higher altitudes) at solar maximum than at solar minimum [e.g., *Cai et al*., 2008]. The International Reference Ionosphere (IRI2012) model gives a peak electron density at Longyearbyen for 09:00 UT of $2.89 \times 10^{11}\,\mathrm{m}^{-3}$ at 300 km altitude in 2003 and $0.676 \times 10^{11}\,\mathrm{m}^{-3}$ at 280 km altitude in 1996. The high ionospheric electron density will have a strong effect on the overlying *F* region critical frequency (f_0F_2) of the ionosphere. Under the assumption that the HF radio wave will achieve orthogonality at the peak electron density, the real raypath will have a stronger refraction and a higher altitude reflection point for solar maximum given the same radar frequency. This means that the mapped range distribution in the first event (2003) would be overestimated using the standard SuperDARN virtual height model, which is consistent with the results presented here.

5.2. Variability With MLT

Within each of the individual case studies, the magnitude of the latitude difference between the two boundaries was also seen as the observations traversed the cusp region from the dawnside to the duskside ionosphere. For the first case study at 08:52–10:00 UT (~11:52–13:00 MLT) the mean latitude difference of 2.28° is about 1° larger than that observed before magnetic noon. For the second case study a smaller mean latitude difference of 1.15° is observed in the afternoon sector (~12:15–14:00 MLT), although this is still 0.75° larger than that observed before magnetic noon. This difference cannot be attributed to uncertainties introduced in the auroral boundary algorithm, as shown by the magnitude of the error bars. The estimated growth time for the gradient drift instability of 10–50 s [*Moen et al*., 2012] and the observed ion Doppler velocity is also too small to explain the 1.15° and 0.75° differences in latitude. Similar signatures have also been identified in previous statistical studies. Through statistical comparisons with Defense Meteorological

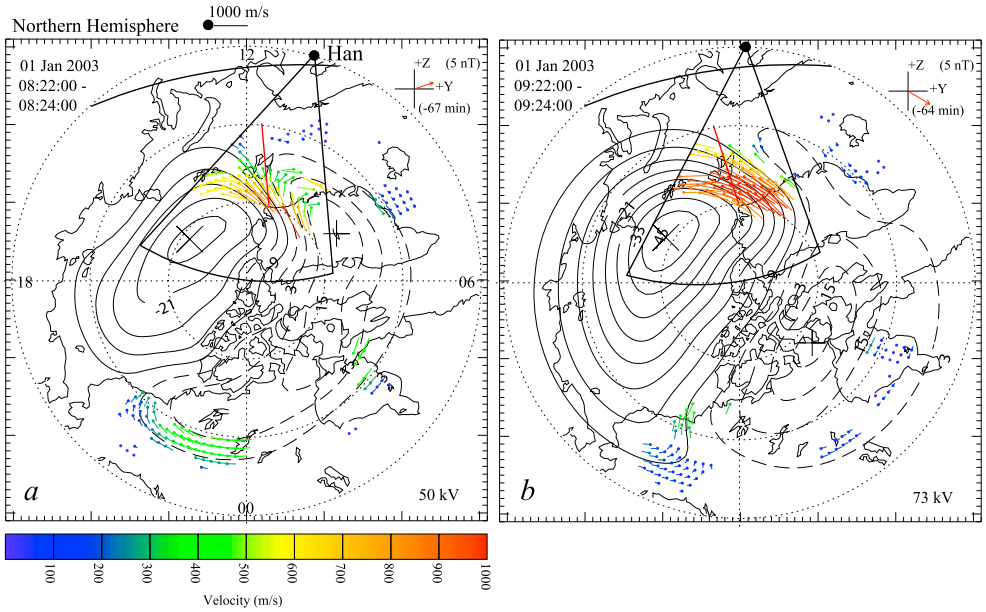

Figure 7. SuperDARN map potential plots showing the Northern Hemisphere ionospheric convection pattern in MLAT/MLT coordinates. 80°, 70°, and 60° MLAT are marked with black dotted lines. The black solid line indicates the field-of-view of the Finland radar, the red line represents the MSP meridian. Magnetic noon is at the top of each panel. The day/night terminator is plotted on the dayside at approximately 63° MLAT.

Satellite Program (DMSP) particle precipitation boundaries in the 09:00–12:00 MLT region (i.e., ~06:00–09:00 UT), *Chisham et al*. [2005c] observed almost identical latitude distributions. When the SWB was poleward of 74° (as the case in this paper), the median value of the particle precipitation boundary distribution was less than 1° latitude difference for the whole 12:00–18:00 MLT interval [*Chisham et al*., 2005a]. This implies that the variable latitude differences with MLT observed in both case studies may be attributed to locally changing background ionospheric densities. To investigate this further, the large-scale plasma flow across the Finland field of view is examined, as any variations in the ionospheric convection pattern will alter the source region of the plasma.

Figure 7 presents two plots of the ionospheric plasma convection in the Northern Hemisphere based on the SuperDARN map potential model [*Ruohoniemi and Baker*, 1998]. A magnetic latitude-magnetic local time (MLAT/MLT) projection is used, the field-of-view of the Finland radar is indicated, and the MSP meridian is denoted by the solid red line. Magnetic noon is located at the top of each panel. The day/night terminator is plotted as the black curve line on the dayside. Color and length of the vectors indicate the magnitude of the flow. The flow pattern in Figure 7a, taken at 08:24 UT, shows a typical poleward movement for weakly northward IMF B_z. Since the IMF clock angle is greater than 40°, the production of open flux does not cease entirely [*Sandholt et al*., 1998]. In Figure 7b, as the radar (and MSP) field of view rotates into the dusk convection cell, a velocity enhancement is observed which correspondence to the IMF B_z southward turning. This indicates that the low-latitude return flow carries extreme ultraviolet (EUV) ionized plasma which is then transported into the cusp region from the dusk sector. The high background ionospheric density inflow from the subauroral zone will increase and thus cause an increase in the magnitude of the latitude difference. This would suggest that (1) the enhanced F_2 peak electron density observed around 12:00 MLT is the result of inflow of high-density plasma driven by the IMF B_y component and (2) the average ionospheric electron density in the postnoon side is also higher than the prenoon side.

In the second case, the largest latitude differences are observed at 10:18, 10:26, and 10:55 UT (as marked by the vertical lines in Figure 6). The increased latitude difference corresponds to negative shifts of IMF B_z and is also associated with simultaneously enhanced poleward drifts. An evolution of the ionospheric convection flow from 09:28–10:30 UT is shown in Figure 8. The panels show the Finland radar line-of-sight velocity at time intervals, indicated at the top left of each panel. The ionospheric cusp region has initially been ignited in the eastward part of the field of view and range gates along the MSP meridian start to observe ionospheric

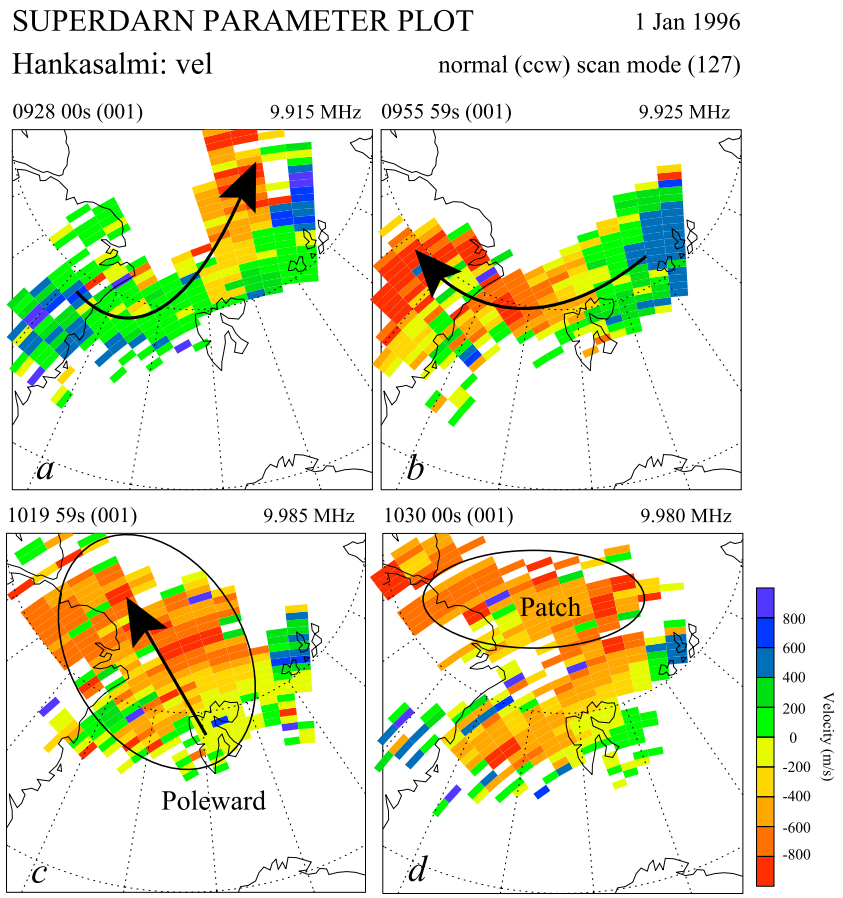

Figure 8. Line-of-sight plasma drift velocity as measured by the SuperDARN radar in Finland on 1 January 1996 at various time intervals from 09:28–10:30 UT. The main features of the flow patterns are identified in each panel.

echoes. The transient plasma drift shown in Figures 8a and 8b appears to be driven by the magnetic tension force exerted by the large IMF B_y component. The ionospheric convection flow has a strong eastward (westward) component before (after) 09:42 UT, as indicated by the black arrows, and is consistent with modulation of the IMF B_y negative (positive) component. Under these conditions, the sunward return flow will be the dominant source for plasma entering into the cusp region [e.g., *Milan et al.*, 2002]. This low density plasma would not change the background ionospheric electron density at the subauroral region; thus, the radar propagation path would be relatively unaffected. This is reflected in the small latitude difference observed in the data (see Figure 6b). Near 10:18 UT (when the IMF becomes increasingly southward) a prominent poleward plasma drift is observed (see Figures 6c and 8c). Under these conditions, the background ionospheric electron density will be replaced by the high-density plasma from the mid or subauroral latitudes [e.g., *Milan et al.*, 2002; *Moen et al.*, 2006]. At 10:30 UT, the first of several high-density patches (an ~$300 \times 700\,\mathrm{km}^2$ wide) were observed to traverse the region (marked in Figure 8d). A sequence of three high-density patches of cold plasma in the subauroral region was studied by *Moen et al.* [2006]. They proposed that reconnection-driven pulsed convection is able to create subauroral patches in the midlatitude region and divert them poleward toward the cusp. When applied to this event, this supports the suggestion that the midlatitude high-density EUV ionized plasma is transported into the HF radar field of view, where it plays a significant role in refracting the radar propagation path. This will, in turn, result in a greater latitude difference between the mapping of the HF radar SWB and the OI 630.0 nm auroral boundary.

6. Conclusion

In this paper, an adjusted method for automatically identifying the HF radar SWB along the MSP meridian has been presented. Using this method, the linear variation of the SWB can be identified with high temporal

resolution. This allows the dynamic evolution in HF radar data to be effectively monitored along the meridian. Using the method of *Johnsen et al*. [2012] for obtaining the open-closed boundary from the cusp OI 630.0 nm auroral emission, the latitude differences between the auroral emission boundary and the HF radar SWB have been compared. Two case studies were used to test the validity of the methods and confirm the existence of mapping errors. The standard SuperDARN virtual height model is one reason for the mapping error [e.g., *Chisham et al*., 2008], while most of the varied latitude differences are more related to the changing background ionospheric electron density. Both the Finland radar and the MSP instrument have simultaneously been operated for more than one solar cycle, and the introduced boundary finding methods will be used for future systematic latitude difference studies.

For the current study, the following conclusions can be made:

1. Due to the fact that the MSP has high spatial resolution near the zenith (where any auroral height ambiguities are negligible), the OI 630.0 nm auroral emission boundary can be used as a "reference location" to derive the average HF radar mapping error.
2. An adjusted method is introduced to identify the radar SWB, which does not require temporal smoothing across several scans, thereby increasing the temporal resolution.
3. The method adheres to the criterion set by *Chisham and Freeman* [2003] that the distributions of spectral width values above (below) the SWB have a Gaussian (exponential) form when 200 m/s was chosen as the threshold value.
4. Given the same HF radar frequency, a higher ionospheric background electron density will cause the HF radar beam path to be refracted at higher altitudes and the standard SuperDARN virtual height model will produce an overestimation of the boundary.
5. Comparing the SWB to optical data from the LYR MSP, the SWB is seen to be on average 0.51° (~56 km) to 1.55° (~170 km) degrees poleward of the optical OCB.
6. The adjusted method outlined in this manuscript is thus a useful tool for identifying the OCB under changing ionospheric conditions in the cusp region using SuperDARN data.

Acknowledgments
The Longyearbyen MSP is owned by the University Centre in Svalbard, and we thank everybody who has been involved in its daily operations. The ACE and WIND IMF and solar wind data were provided by the CDAWeb service (http://cdaweb.gsfc.nasa.gov). We also thank the SuperDARN PIs for the use of the SuperDARN radar data. This project has been supported by the Research Council of Norway under contracts 223252, 212014, 208006, and 230996.

References

Baker, K. B., and S. Wing (1989), A new magnetic coordinate system for conjugate studies at high latitudes, *J. Geophys. Res.*, *94*(A7), 9139–9143, doi:10.1029/JA094iA07p09139.

Baker, K. B., R. A. Greenwald, A. D. M. Walker, P. F. Bythrow, L. J. Zanetti, T. A. Potemra, D. A. Hardy, F. J. Rich, and C. L. Rino (1986), A case study of plasma processes in the dayside cleft, *J. Geophys. Res.*, *91*(A3), 3130–3144, doi:10.1029/JA091iA03p03130.

Baker, K. B., R. A. Greenwald, J. P. Villian, and S. Wing (1988), Spectral characteristics of high frequency (HF) backscatter for high-latitude ionospheric irregularities: Preliminary analysis of statistical properties, Tech. Rep., Johns Hopkins Univ. Appl. Phys. Lab., Laurel, Md.

Baker, K. B., J. R. Dudeney, R. A. Greenwald, M. Pinnock, P. T. Newell, A. S. Rodger, N. Mattin, and C. I. Meng (1995), HF radar signatures of the cusp and low-latitude boundary layer, *J. Geophys. Res.*, *100*(A5), 7671–7695, doi:10.1029/94JA01481.

Baker, K. B., A. S. Rodger, and G. Lu (1997), HF-radar observations of the dayside magnetic merging rate: A Geospace Environment Modeling boundary layer campaign study, *J. Geophys. Res.*, *102*(A5), 9603–9617, doi:10.1029/97JA00288.

Cai, H. T., S. Y. Ma, Y. Fan, Y. C. Liu, and K. Schlegel (2008), Climatological features of electron density in the polar ionosphere from long-term observations of EISCAT/ESR radar, *Ann. Geophys.*, *25*(12), 2561–2569, doi:10.5194/angeo-25-2561-2007.

Chisham, G., and M. . P. Freeman (2003), A technique for accurately determining the cusp-region polar cap boundary using SuperDARN HF radar measurements, *Ann. Geophys.*, *21*(4), 983–996, doi:10.5194/angeo-21-983-2003.

Chisham, G., M. Pinnock, and A. S. Rodger (2001), The response of the HF radar spectral width boundary to a switch in the IMF B_y direction: Ionospheric consequences of transient dayside reconnection?, *J. Geophys. Res.*, *106*(A1), 191–202, doi:10.1029/2000JA900094.

Chisham, G., M. P. Freeman, M. M. Lam, G. A. Abel, T. Sotirelis, R. A. Greenwald, and M. Lester (2005a), A statistical comparison of SuperDARN spectral width boundaries and DMSP particle precipitation boundaries in the afternoon sector ionosphere, *Ann. Geophys.*, *23*(12), 3645–3654, doi:10.5194/angeo-23-3645-2005.

Chisham, G., M. P. Freeman, T. Sotirelis, and R. A. Greenwald (2005b), The accuracy of using the spectral width boundary measured in off-meridional SuperDARN HF radar beams as a proxy for the open-closed field line boundary, *Ann. Geophys.*, *23*(12), 2599–2604, doi:10.5194/angeo-23-2599-2005.

Chisham, G., M. P. Freeman, T. Sotirelis, R. A. Greenwald, M. Lester, and J. P. Villain (2005c), A statistical comparison of SuperDARN spectral width boundaries and DMSP particle precipitation boundaries in the morning sector ionosphere, *Ann. Geophys.*, *23*(3), 733–743, doi:10.5194/angeo-23-733-2005.

Chisham, G., et al. (2007), A decade of the Super Dual Auroral Radar Network (SuperDARN): Scientific achievements, new techniques and future directions, *Surv. Geophys.*, *28*(1), 33–109, doi:10.1007/s10712-007-9017-8.

Chisham, G., T. K. Yeoman, and G. Sofko (2008), Mapping ionospheric backscatter measured by the SuperDARN HF radars–Part 1: A new empirical virtual height model, *Ann. Geophys.*, *26*(4), 823–841, doi:10.5194/angeo-26-823-2008.

Cowley, S. W. H., and M. Lockwood (1992), Excitation and decay of solar wind-driven flows in the magnetosphere-ionophere system, *Ann. Geophys.*, *10*, 103–115.

Dungey, J. W. (1961), Interplanetary magnetic field and the auroral zones, *Phys. Rev. Lett.*, *6*(2), 47–48, doi:10.1103/PhysRevLett.6.47.

Greenwald, R. A., et al. (1995), DARN/SuperDARN: A global view of the dynamics of high-latitude convection, *Space Sci. Rev.*, *71*(1–4), 761–796, doi:10.1007/BF00751350.

Johnsen, M. G., and D. A. Lorentzen (2012), The dayside open/closed field line boundary as seen from space and ground-based instrumentation, *J. Geophys. Res.*, *117*, A03320, doi:10.1029/2011JA016983.
Johnsen, M. G., D. A. Lorentzen, J. M. Holmes, and U. P. Løvhaug (2012), A model based method for obtaining the open/closed field line boundary from the cusp auroral 6300 Å[OI] red line, *J. Geophys. Res.*, *117*, A03319, doi:10.1029/2011JA016980.
Lei, J., L. Liu, W. Wan, S.-R. Zhang, and A. P. van Eyken (2006), Comparison of the first long-duration IS experiment measurements over Millstone Hill and EISCAT Svalbard radar with IRI2001, *Adv. Space Res.*, *37*(5), 1102–1107, doi:10.1016/j.asr.2005.01.061.
Liou, K., P. T. Newell, C.-I. Meng, M. Brittnacher, and G. Parks (1998), Characteristics of the solar wind controlled auroral emissions, *J. Geophys. Res.*, *103*(A8), 17,543–17,557, doi:10.1029/98JA01388.
Liu, E. X., H. Q. Hu, R. Y. Liu, Z. S. Wu, and M. Lester (2012), An adjusted location model for SuperDARN backscatter echoes, *Ann. Geophys.*, *30*(12), 1769–1779, doi:10.5194/angeo-30-1769-2012.
Lockwood, M. (1998), Identifying the open-closed field line boundary, in *Polar Cap Boundary Phenomena*, edited by J. Moen et al., pp. 73, Kluwer Acad., Norwell, Mass.
Lockwood, M., P. E. Sandholt, S. W. H. Cowley, and T. Oguti (1989), Interplanetary magnetic field control of dayside auroral activity and the transfer of momentum across the dayside magnetopause, *Planet. Space Sci.*, *37*(11), 1347–1365, doi:10.1016/0032-0633(89)90106-2.
Lockwood, M., H. C. Carlson Jr., and P. E. Sandholt (1993), Implications of the altitude of transient 630-nm dayside auroral emissions, *J. Geophys. Res.*, *98*(A9), 15,571–15,587, doi:10.1029/93JA00811.
Lorentzen, D. A., and J. Moen (2000), Auroral proton and electron signatures in the dayside aurora, *J. Geophys. Res.*, *105*(A6), 12,733–12,745, doi:10.1029/1999JA900405.
Lorentzen, D. A., C. S. Deehr, J. I. Minow, R. W. Smith, H. C. Stenbaek-Neielsen, F. Sigernes, R. L. Arnoldy, and K. Lynch (1996), SCIFER-Dayside auroral signatures of magnetospheric energetic electrons, *Geophys. Res. Lett.*, *23*(14), 1885–1888, doi:10.1029/96GL00593.
Milan, S. E., M. Lester, S. W. H. Cowley, J. Moen, P. E. Sandholt, and C. J. Owen (1999), Meridian-scanning photometer, coherent HF radar, and magnetometer observations of the cusp: A case study, *Ann. Geophys.*, *17*(2), 159–172, doi:10.1007/s005850050746.
Milan, S. E., M. Lester, and T. K. Yeoman (2002), HF radar polar patch formation revisited: Summer and winter variations in dayside plasma structuring, *Ann. Geophys.*, *20*(4), 487–499, doi:10.5194/angeo-20-487-2002.
Moen, J., D. A. Lorentzen, and F. Sigernes (1998), Dayside moving auroral forms and bursty proton auroral events in relation to particle boundaries observed by NOAA 12, *J. Geophys. Res.*, *103*(A7), 14,855–14,863, doi:10.1029/97JA02877.
Moen, J., H. C. Carlson, S. E. Milan, N. Shumilov, B. Lybekk, P. E. Sandholt, and M. Lester (2001), On the collocation between dayside auroral activity and coherent HF radar backscatter, *Ann. Geophys.*, *8*(12), 1531–1549, doi:10.1007/s00585-001-1531-2.
Moen, J., H. C. Carlson, K. Oksavik, C. P. Nielsen, S. E. Pryse, H. R. Middleton, I. W. McCrea, and P. Gallop (2006), EISCAT observations of plasma patches at sub-auroral cusp latitudes, *Ann. Geophys.*, *24*(9), 2363–2374, doi:10.5194/angeo-24-2363-2006.
Moen, J., X. C. Qiu, H. C. Carlson, R. Fujii, and I. W. McCrea (2008a), On the diurnal variability in F2-region plasma density above the EISCAT Svalbard radar, *Ann. Geophys.*, *26*, 2427–2433, doi:10.5194/angeo-26-2427-2008.
Moen, J., Y. Rinne, H. C. Carlson, K. Oksavik, R. Fujii, and H. Opgenoorth (2008b), On the relationship between thin Birkeland current arcs and reversed flow channels in the winter cusp/cleft ionosphere, *J. Geophys. Res.*, *113*, A09220, doi:10.1029/2008JA013061.
Moen, J., K. Oksavik, T. Abe, M. Lester, Y. Saito, T. A. Bekkeng, and K. S. Jacobsen (2012), First in-situ measurements of HF radar echoing targets, *Geophys. Res. Lett.*, *39*, L07104, doi:10.1029/2012GL051407.
Newell, P. T., and C.-I. Meng (1988), The cusp and the cleft/boundary layer: Low-altitude identification and statistical local time variation, *J. Geophys. Res.*, *93*(A12), 14,549–14,556, doi:10.1029/JA093iA12p14549.
Øieroset, M., P. E. Sandholt, H. Lühr, W. F. Denig, and T. Moretto (1997), Auroral and geomagnetic events at cusp/mantle latitudes in the prenoon sector during positive IMF B_y conditions: Signatures of pulsed magnetopause reconnection, *J. Geophys. Res.*, *102*(A4), 7191–7205, doi:10.1029/96JA03716.
Oksavik, K., J. Moen, and H. C. Carlson (2004a), High-resolution observations of the small-scale flow pattern associated with a poleward moving auroral form in the cusp, *Geophys. Res. Lett.*, *31*, L11807, doi:10.1029/2004GL019838.
Oksavik, K., F. Søraas, J. Moen, R. Pfaff, J. A. Davies, and M. Lester (2004b), Simultaneous optical, CUTLASS HF radar, and FAST spacecraft observations: Signatures of boundary layer processes in the cusp, *Ann. Geophys.*, *22*(2), 511–525, doi:10.5194/angeo-22-511-2004.
Oksavik, K., J. Moen, H. C. Carlson, R. A. Greenwald, S. E. Milan, M. Lester, W. F. Denig, and R. J. Barnes (2005), Multi-instrument mapping of the small-scale flow dynamics related to a cusp auroral transient, *Ann. Geophys.*, *23*(7), 2657–2670, doi:10.5194/angeo-23-2657-2005.
Oksavik, K., J. I. Moen, E. H. Rekaa, H. C. Carlson, and M. Lester (2011), Reversed flow events in the cusp ionosphere detected by SuperDARN HF radars, *J. Geophys. Res.*, *116*, A12303, doi:10.1029/2011JA016788.
Oksavik, K., J. Moen, M. Lester, T. A. Bekkeng, and J. K. Bekkeng (2012), In situ measurements of plasma irregularity growth in the cusp ionosphere, *J. Geophys. Res.*, *117*, A11301, doi:10.1029/2012JA017835.
Pinnock, M., and A. S. Rodger (2001), On determining the noon polar cap boundary from SuperDARN HF radar backscatter characteristics, *Ann. Geophys.*, *18*(12), 1523–1530, doi:10.1007/s00585-001-1523-2.
Pinnock, M., A. S. Rodger, K. B. Baker, G. Lu, and M. Hairston (1999), Conjugate observations of the day-side reconnection electric field: A GEM boundary layer campaign, *Ann. Geophys.*, *17*(4), 443–454, doi:10.1007/s00585-999-0443-4.
Ponomarenko, P. V., and C. L. Waters (2006), Spectral width of SuperDARN echoes: Measurement, use and physical interpretation, *Ann. Geophys.*, *24*(1), 115–128, doi:10.5194/angeo-24-115-2006.
Ponomarenko, P. V., C. L. Waters, and F. W. Menk (2007), Factors determining spectral width of HF echoes from high latitudes, *Ann. Geophys.*, *25*(3), 675–687, doi:10.5194/angeo-25-675-2007.
Rees, M. H. (1963), Auroral ionization and excitation by incident energetic electrons, *Planet. Space Sci.*, *11*(10), 1209–1218, doi:10.1016/0032-0633(63)90252-6.
Rees, M. H. (1989), *Physics and Chemistry of the Upper Atmosphere*, Cambridge Univ. Press, Cambridge, U. K.
Rinne, Y., J. Moen, K. Oksavik, and H. C. Carlson (2007), Reversed flow events in the winter cusp ionosphere observed by the European Incoherent Scatter (EISCAT) Svalbard radar, *J. Geophys. Res.*, *112*, A10313, doi:10.1029/2007JA012366.
Rodger, A. S., S. B. Mende, T. J. Rosenberg, and K. B. Baker (1995), Simultaneous optical and HF radar observations of the ionospheric cusp, *Geophys. Res Lett.*, *22*(15), 2045–2048, doi:10.1029/95GL01797.
Romick, G. J. (1976), The detection and study of the visible spectrum of the aurora and airglow, in *Proc. SPIE*, *Methods Atmos. Radiometry*, vol. 0091, pp. 63–70, Alaska, Univ., Fairbanks, Alaska, doi:10.1117/12.955072.
Ruohoniemi, J. M., and K. B. Baker (1998), Large-scale imaging of high-latitude convection with Super Dual Auroral Radar Network HF radar observations, *J. Geophys. Res.*, *103*(A9), 20,797–20,811, doi:10.1029/98JA01288.
Sandholt, P. E., C. J. Farrugia, J. Moen, Ø. Noraberg, B. Lybekk, T. Sten, and T. Hansen (1998), A classification of dayside auroral forms and activities as a function of interplanetary magnetic field orientation, *J. Geophys. Res.*, *103*(A10), 23,325–23,345, doi:10.1029/98JA02156.

Sandholt, P. E., C. J. Farrugia, S. W. H. Cowley, and M. Lester (2001), Dayside auroral bifurcation sequence during *B y* -dominated interplanetary magnetic field: Relationship with merging and lobe convection cells, *J. Geophys. Res.*, *106*(A8), 15,429–15,444, doi:10.1029/2000JA900161.

Solomon, S. C., P. B. Hays, and V. J. Abreu (1988), The auroral 6300 Å emission: Observations and modeling, *J. Geophys. Res.*, *93*, 9867–9882, doi:10.1029/JA093iA09p09867.

Villain, J. P., R. A. Greenwald, and J. F. Vickrey (1984), HF ray tracing at high latitudes using measured meridional electron density distributions, *Radio Sci.*, *19*(1), 359–374, doi:10.1029/RS019i001p00359.

Villain, J. P., R. André, M. Pinnock, R. A. Greenwald, and C. Hanuise (2002), A statistical study of the Doppler spectral width of high-latitude ionospheric F-region echoes recorded with SuperDARN coherent HF radars, *Ann. Geophys.*, *20*(11), 1769–1781.

Yeoman, T. K., M. Lester, S. W. H. Cowley, S. E. Milan, J. Moen, and P. E. Sandholt (1997), Simultaneous observations of the cusp in optical, DMSP and HF radar data, *Geophys. Res. Lett.*, *24*(17), 2251–2254, doi:10.1029/97GL02072.

Yeoman, T. K., D. M. Wright, A. J. Stocker, and T. B. Jones (2001), An evaluation of range accuracy in the Super Dual Auroral Radar Network over-the-horizon HF radar systems, *Radio Sci.*, *36*(4), 801–813, doi:10.1029/2000RS002558.

Yeoman, T. K., G. Chisham, L. J. Baddeley, R. S. Dhillon, T. J. T. Karhunen, T. R. Robinson, A. Senior, and D. M. Wright (2008), Mapping ionospheric backscatter measured by the SuperDARN HF radars-Part 2: Assessing SuperDARN virtual height models, *Ann. Geophys.*, *26*(4), 843–852, doi:10.5194/angeo-26-843-2008.

Zhang, S.-R., J. M. Holt, D. K. Bilitza, T. van Eyken, M. McCready, C. Amory-Mazaudier, S. Fukao, and M. Sulzer (2007), Multiple-site comparisons between models of incoherent scatter radar and IRI, *Adv. Space Res.*, *39*(5), 910–917, doi:10.1016/j.asr.2006.05.027.